JOURNAL OF AIRCRAFT
Vol. 42, No. 5, September–October 2005

# Novel Hierarchical Modular Control Methodology for Closed-Loop Flow-Control Applications

Mehul P. Patel,* Richard M. Kolacinski,† and Troy S. Prince‡
*Orbital Research, Inc., Cleveland, Ohio 44103*
T. Terry Ng§
*University of Toledo, Toledo, Ohio 43606*
and
James H. Myatt¶
*U.S. Air Force Research Laboratory, Wright–Patterson Air Force Base, Ohio 45433*

**A novel hierarchical modular control methodology using closed-loop flow control for active virtual shaping of aerodynamic surfaces is developed. Through wind tunnel experimentation and numerical simulation, we show that collocated sensor–actuator pairs and closed-loop feedback control can effectively modulate the local flow phenomenon and, furthermore, by coordinating the local flow phenomenon, macroscopic force and moment effects can be induced on the aerodynamic surface. The results of flow experiments at Mach 0.08 on a two-dimensional airfoil are used to construct a dynamic model of the effect of discrete suction actuators, and a closed-loop adaptive control system is designed to modulate the local flow phenomenon based on this model. A feedforward control system is then constructed to coordinate the behavior of multiple intelligent control modules, each composed of a collocated sensor–actuator pair and a closed-loop control system. In conclusion, we use a full six-degree-of-freedom numerical simulation to investigate the application of the aggregate system to tracking desired rolling and pitching moment trajectories via actuator-induced aeroshaping of the aerodynamic surfaces of an aircraft.**

## I. Introduction

UNPRECEDENTED levels of air vehicle performance will be required to meet mission-specific objectives in the combat arenas of the near future. To accomplish this, future air vehicles will need to be highly maneuverable, stealthy, and reliable. These air vehicles will be required to maintain their ability to control and maneuver with limited or even no use of traditional (hinged) control surfaces. Some air vehicles with unconventional designs (nonaerodynamic surfaces) may be needed for carrying certain types of sensors and armament. It is possible that advanced control techniques will be required to enable new air vehicle designs that retain and improve their aerodynamic efficiency, even without the full use of traditional control surfaces.

Closed-loop flow control offers great potential in revolutionizing the flying capabilities of air vehicles by means of virtual aerodynamic shaping. Virtual shaping of an aerodynamic surface refers to the modification of the flowfield around the surface by means of mass/momentum/energy transfer, which results in the fluid flowing around the surface as if the surface geometry is altered. This modified flowfield leads to a desired change in aerodynamic forces and moments. Consequently, virtual aerodynamic shaping has the potential to enable air vehicle designs that are dictated by mission-specific requirements as well as aerodynamic performance requirements.

### A. Flow-Control Work

In recent years, the advent of smart actuators based on technologies such as piezoelectric materials, microelectromechanical systems, and shape memory alloys led to the development of various devices to provide control to air vehicles by altering local aerodynamic flow phenomena. One of the most significant characteristics of these devices is the ability to induce perturbations at critical locations in the flowfields to effect a desired change. This enables the concept of an adaptive virtual aerodynamic surface that can be tailored to different operating conditions. One of the potential applications of such technology is in the development of unmanned aerial vehicles without conventional control surfaces for maneuvering with low observability, reduced drag/weight, and design flexibility. This technology also has a logical application to air vehicles where the functional requirements dictate a nonaerodynamic shape. As such, a significant improvement in the aerodynamic control and efficiency is needed and can be obtained through active flow control.

Some of the flow-control actuators recently investigated are zero-net-mass synthetic jets, pulsed slot blowing, deployable vortex generators, vortex-generating jets, and discrete suction.[1–5] Although the basic principles behind these controls can be quite different, they all share one thing in common: the ability to control boundary-layer separation. The key advantage of a separation-based control is that very large control forces can be generated using devices that are potentially small in size, lightweight, and less mechanically complex than other controls such as a variable-camber airfoil. In general, the successful application of these actuators relies heavily on flow-sensors and closed-loop flow-control strategies.

### B. Flow Sensing

Sensors are critical to the design of a closed-loop flow-control system because they provide crucial information on the sublayer flowfield required for the design and tuning of the closed-loop feedback controller. In practice, sensors for use with flow-control applications need to be robust, nonintrusive, and usable on a flying vehicle; therefore, they need to be flush-mounted. The most commonly used sensors for flow measurement are dynamic (fast response) pressure sensors and/or shear stress sensors. In this study, fast-response pressure sensors with a sampling rate of 500 Hz are used in conjunction with static pressure ports.

---

Received 4 December 2003; revision received 7 March 2005; accepted for publication 7 March 2005.

*Director, Aerodynamics Group, 4415 Euclid Avenue, Suite 500. Senior Member AIAA.

†Director, Advanced Controls Group, 4415 Euclid Avenue, Suite 500. Member AIAA.

‡Vice President of Technology, 4415 Euclid Avenue, Suite 500. Member AIAA.

§Professor, Department of Mechanical, Industrial, and Manufacturing Engineering, Nitschke Hall 4061. Senior Member AIAA.

¶Senior Aerospace Engineer, 2210 8th Street, Building 146, Room 300. Senior Member AIAA.

### C. Closed-Loop Flow Control

The control of unsteady aerodynamics can only be accomplished through the use of a closed-loop control system. An extensive body of work on separation control phenomena and closed-loop controller design, using both experimental and computational fluid dynamics models, exists in the literature. The literature includes traditional control algorithms based on both linear and nonlinear approximations to Navier–Stokes equations as well as nontraditional approaches such as neural networks.[6–8] Despite the size of this body of work, practical feedback controllers have not yet been developed for active flow-control applications such as aerodynamic shaping for lifting surfaces.

Work reported by Patel et al.[3] demonstrates the use of minute active flow-control modules, each consisting of a collocated sensor–actuator pair and a processor for implementing feedback control. These intelligent control modules (ICMs) are shown to be capable of actively controlling localized flow separation on a pitching NACA 0020 wing at a Reynolds number of $0.6 \times 10^6$.[3,9] In this paper, we investigate the development of a hierarchical flow-control approach that uses a global control system (GCS) to coordinate these ICMs. It should be noted that the control system architecture presented is not predicated upon the use of any specific design methodology for the construction of either the ICMs or the GCS. Rather, the architecture presented here provides a framework within which a control system designer may independently construct ICM control laws and a coordinating GCS using the methodologies that are most appropriate to their specific application.

## II. Closed-Loop Control Architecture

The architecture of the flow-control system is decomposed into two levels. The lower level is composed of multiple local or minor-loop feedback controllers that modulate the lift over discrete wing sections and track the lift trajectories supplied by the GCS. The logic/control laws for the local controllers are resident within the ICMs and, excepting performance requirements assumed by the GCS, are not dependent on the design of the GCS. The outer or major loop of the control architecture is the GCS, which takes as input the desired body moments and supplies as output the spanwise lift distribution for the wing, which is necessary to achieve the desired moments. Furthermore, the GCS may be either centralized or distributed and, therefore, its logic may also be resident within the ICMs. The architecture of this control system is somewhat analogous to that of the guidance and control loops of an autopilot system.

For the purposes of this study, a two-dimensional airfoil is used and therefore it is assumed that no spanwise flow exists on the surface of the airfoil. The present closed-loop control system is designed for air vehicles with high-aspect-ratio control surfaces where it is assumed that the lift generated by an airfoil section is independent of the lift generated by all other airfoil sections. Under this assumption, the total lift produced by the airfoil is equal to the sum of the lift forces generated by the separate airfoil sections. By modulating the lift generation of the airfoil sections, the net lift force and the spanwise center of pressure may be modulated independently. The pitching moment is then a linear function of the net lift produced, and the rolling moment is a function of the net lift force and the spanwise location of the center of pressure.

As noted in the prequel, the architecture presented here does not presuppose any specific control methodologies for the design of either the GCS or the ICMs. For the purposes of this study, it is assumed that the transient behavior of the aerodynamics on each of the spanwise sections can be captured by a linear, time-varying model. Moreover, it is assumed that the parameters of the linear model vary slowly and, hence, the parametric changes associated with changing aerodynamic conditions may be dealt with via a self-tuning regulator (STR).[10]

In the following sections, we present analytical and experimental development of the aerodynamic model and the development and simulation of the control architecture.

## III. Wind-Tunnel Experiments

### A. Airfoil Model

Figure 1 provides an illustration of the closed-loop flow-control system utilizing discrete ICMs on an airfoil. The experimental work presented here uses a two-dimensional airfoil model with 19.05-cm chord, $c$, and 30.48-cm span (Fig. 2) in a 0.9 × 0.9 m closed-loop, low-speed wind tunnel at the University of Toledo. The airfoil model is intentionally designed with an abrupt expansion reflex (wedge) near the trailing edge at $0.8c$ to force natural flow separation at low angles of attack. Static and dynamic measurements of static pressure are made using 16 slow-response sensors and 8 fast-response pressure sensors located on the upper surface of the airfoil as shown

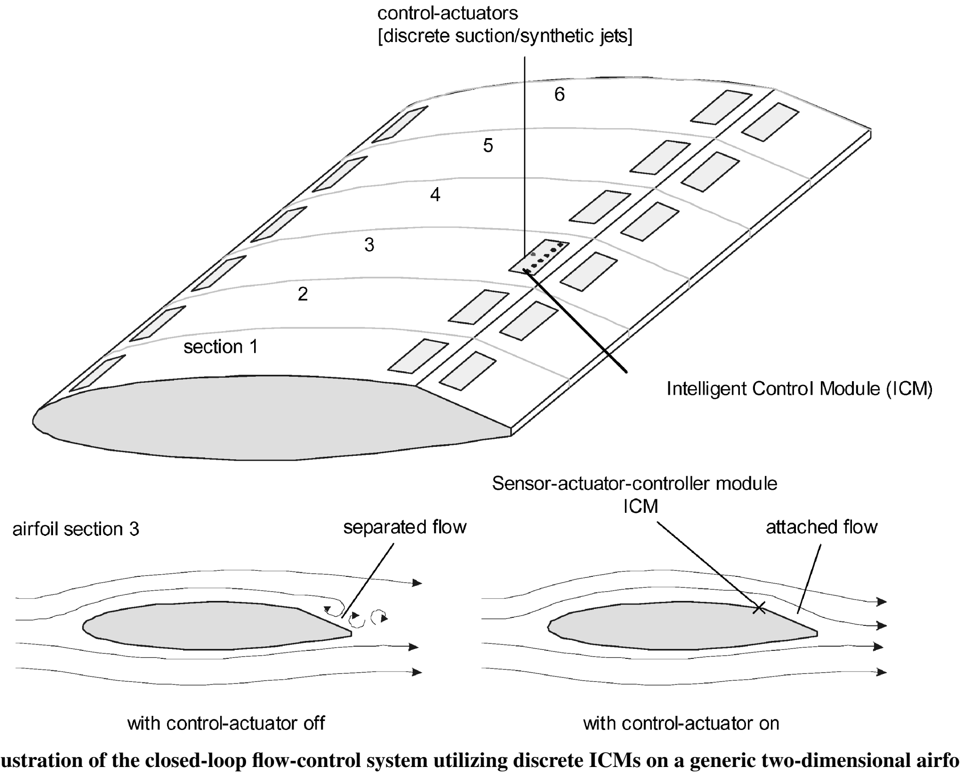

**Fig. 1 Illustration of the closed-loop flow-control system utilizing discrete ICMs on a generic two-dimensional airfoil model.**

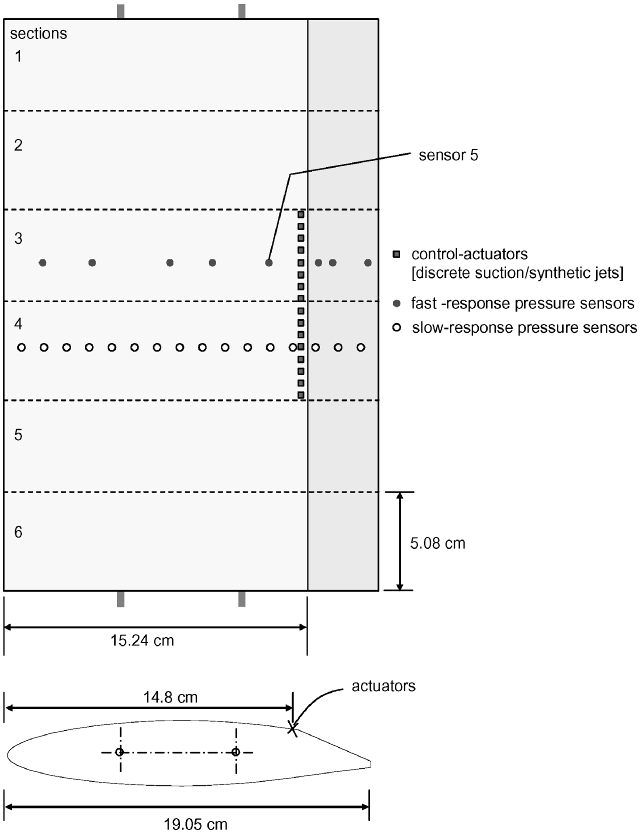

**Fig. 2 Two-dimensional airfoil model with sensors and actuators on sections 3 and 4.**

in Fig. 2. Another row of 16 slow-response pressure ports is located on the lower surface of the airfoil.

### B. Discrete Suction: Control Actuator Scheme

Discrete suction was used as the actuator on the two-dimensional airfoil. Tubing was attached to both ends of an internal chamber in the airfoil to facilitate suction through a suction pump, and the suction rate was monitored using a Hasting electronic mass flow meter. Controlled perturbations were employed from a series of holes of 1 mm diameter each, located spanwise on the airfoil section (sec. 3 in Fig. 2) at $0.77c$. The low-energy perturbation triggers instabilities in the flowfield near the boundary layer, which energize the flow within the boundary layer resulting in a delay in flow separation. It has been shown in previous studies that different levels of effectiveness can be achieved by varying the suction pattern and suction levels, $C_m$, formed by a group of activated holes[11–13]: $C_m = \dot{m}/(\rho \times U \times S_{\text{ref}})$, where $\dot{m}$ is the mass flow rate, $\rho$ is the density of air, $U$ is the freestream velocity, and $S_{\text{ref}}$ is the surface area of the airfoil. For practical considerations, only low suction levels ($C_m \sim 10^{-4}$) are considered in this study.

### C. Steady and Unsteady Experiments

In the work reported here, the effect of discrete suction through spanwise holes located at $0.77c$ is quantified at a Reynolds number of $0.35 \times 10^6$ for angles of attack ranging from $-2$ to 12 deg in increments of 2 deg. Figures 3 and 4 show the effect of discrete suction on the pressure distribution, $C_p$, where $C_p = (P_0 - P_\infty)/q_\infty$ and $P_0$ is the local static pressure, $P_\infty$ is the ambient static pressure, and $q_\infty$ is the dynamic pressure, over the upper and lower surfaces of the two-dimensional airfoil. Sharp suction peaks upstream of the reflex at $0.8c$ in Fig. 3 (panels a–d) demonstrate the significant control effect possible by using discrete suction for $-2$ to 4 deg $\alpha$. Panels e and f of Fig. 3, however, show that the control effect is negligible for $\alpha > 4$ deg. This is due to regions of flow separation near the reflex line and the inability of the control actuators to completely reattach the flow. Plots of $C_p$ vs angle of attack ($-2$ to 12 deg) at different chord locations ($0.66c$, $0.72c$, $0.78c$) located upstream of the reflex point at $0.8c$ demonstrate similar $C_p$ characteristics for baseline and discrete suction, as shown in Fig. 4 (panels a–c). Figure 4 (panel d) shows pressure distribution vs angle of attack on the upper surface aft of the reflex line at $0.8c$. It can be seen that, due to the low suction rate ($C_m = 0.00172$), the effect of discrete suction is reduced at high angle of attack where there is massive separation upstream of the reflex line at $0.8c$. Increasing the suction rate would force the flow to reattach and improve the airfoil's aerodynamic performance. Figure 5 shows lift coefficient ($C_L$) and pitching moment ($C_M$) vs angle of attack for baseline (no suction) and maximum suction rate (i.e., $C_m = 0.00172$). These experiments demonstrate that discrete suction can be effectively used to obtain sufficient resolution for controller development, as shown in Fig. 6.

To design a closed-loop control system, it is necessary to obtain the transient response of the actuator on the flowfield. In addition, data from steady and dynamic (step-response) experiments at different angle-of-attack ($-4$ to 6 deg) provide the actuator saturation limits. Pressure variations over the surface of the two-dimensional airfoil are used to obtain the saturation limits at different angle-of-attack conditions and at different suction rates, $C_m$.

Characteristic plots obtained from steady $C_m$-modulation experiments at different angle-of-attack conditions are similar to the plots presented in Fig. 6. Actuator on/off tests for 4–6-deg angle of attack at similar flow conditions provide the transient and steady-state responses to actuation associated with the flow dynamics. Figure 7 presents the dynamic flowfield response observed at pressure sensor 5. Figures 8 and 9 show details of the dynamic flowfield response and illustrate the transient response to step changes in actuation. In most instances, the actuator response time (i.e., the time it takes for the local pressure to stabilize after the actuator has been turned either on or off) was $\sim 0.04$ s. Data from these experiments provide an empirical basis for a linear model of the discrete suction actuator. Results from the two-dimensional airfoil were used to estimate the control-induced lift increment on the three-dimensional wing used in our simulation. The estimation is reasonable over a significant portion of the span of a wing with small sweep and at low angles of attack. Furthermore, when applying to a three-dimensional wing, the discrete holes, reflex point, and trailing edge will be shaped and aligned to the main flow over the wing to retain a pseudo-two-dimensional behavior. At high sweeps and angles of attack, the flow will be dominated by vortices, and the type of control used will need to be altered.

## IV. Global Control System

It is assumed that ICMs are located spanwise across an airfoil section of length $L$, such as in sec. 3 in Fig. 2. The global controller modulates the net force and center of pressure location by varying the weighting of predetermined lift distributions spanwise along the controllable sections of the airfoil. As discussed previously, each ICM is controlled by an STR. A pole placement algorithm is used to implement the STR and, within actuation bounds, each ICM and its associated wing section appears to possess identical dynamics from the perspective of the GCS. The assignment of identical closed-loop dynamics to each wing section greatly simplifies the design and construction of the GCS.

In the implementation of the hierarchical control system presented here, a distribution for an increment to the base lift force along the airfoil section is constructed from the superposition of two shape functions: a spanwise constant bias and a linearly varying distribution depicted in Fig. 10. The shape of the lift distribution and, hence, the net lift and location of the center of pressure is controlled by adjusting the weights on the component shape functions. The selection of this set of shape functions reflects the assignment of identical closed-loop dynamics to each ICM and the underlying linearity of the airfoil model assumptions. As such, these shape functions are not optimal for a more detailed airfoil model or relaxation of the model assumptions.

The lift force increment is in addition to the nominal lift force produced by the airfoil for a given flow condition (i.e., angle of attack). It is assumed that the nominal lift forces by the wings on either side of the aircraft are equal and, hence, do not contribute to

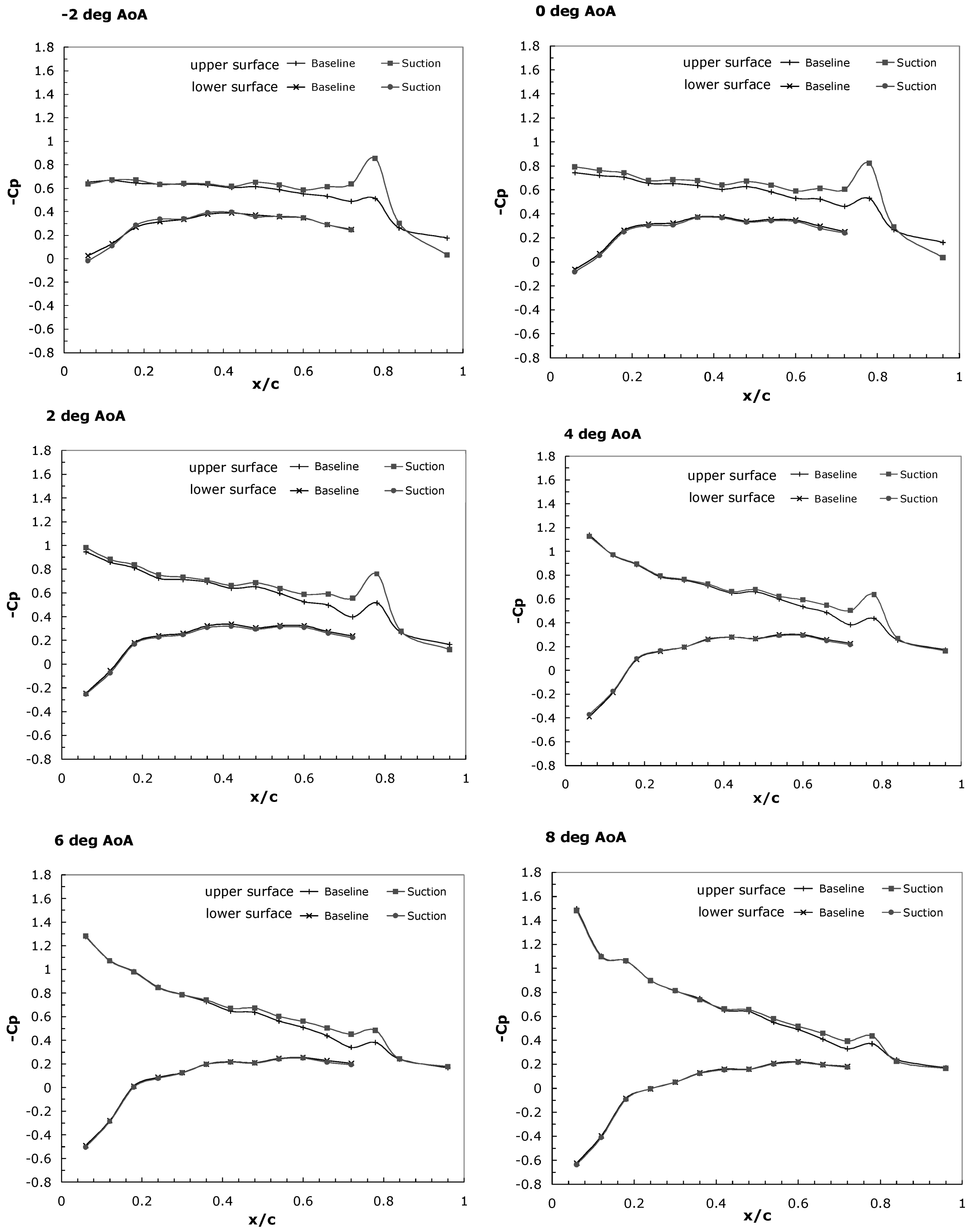

Fig. 3 Effects of discrete suction ($C_m = 0.00172$) on the pressure coefficient along the two-dimensional wing chord for different angles of attack.

the moments about the center of mass of the aircraft. Neglecting the effects of other control surfaces, the moments about the center of mass of the aircraft are solely due to the lift increments produced by the ICMs and therefore, without loss of generality, it may be assumed that the nominal lift is zero. It is assumed that the center of pressure on the two-dimensional (unswept) airfoil is constrained to lie on a line parallel to the leading and trailing edges of the airfoil. Consequently, varying the lift distribution spanwise along the airfoil allows modulation of both the net lift produced by the airfoil and the spanwise location of the center of pressure along the center-of-pressure line. The current incarnation of the GCS assumes that the center-of-pressure line lies normal to the plane of symmetry of the vehicle to which the airfoil is attached and that the aircraft's center of mass does not lie on the center-of-pressure line, as shown in Fig. 11. Physically this would resemble any unswept lifting/control surface on a traditional aircraft.

Let $l_p$ be the distance between the aircraft center of mass and the center-of-pressure line, $l_r$ be the distance from the aircraft's plane of symmetry to the center of pressure, and $F_l$ be the net lift force acting through the center of pressure. Assuming a standard aircraft coordinate system with its origin coincident with the center of mass, $x$ axis directed out through the nose of the aircraft, $y$ axis directed outward, parallel to the starboard wing, and $z$ axis directed downward through the belly of the aircraft, the pitching

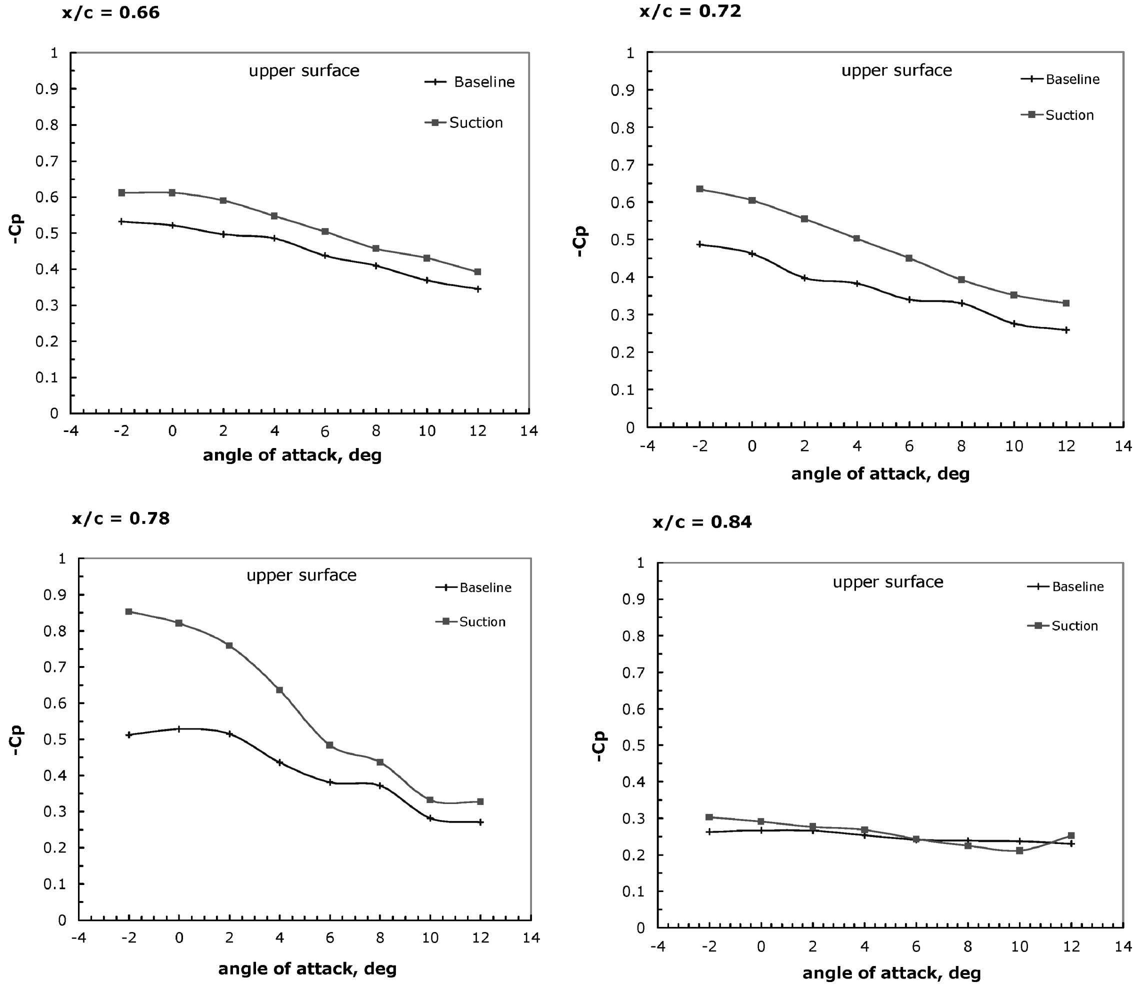

**Fig. 4 Effects of discrete suction ($C_m = 0.00172$) on the pressure coefficient along the two-dimensional wing chord for different angles of attack.**

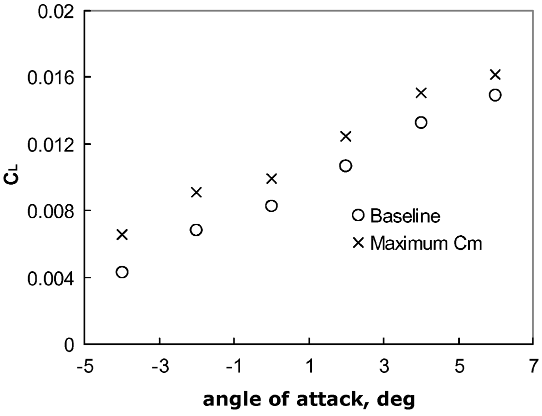

**Fig. 5 Lift coefficient vs angle of attack for baseline (no suction) and maximum suction ($C_m = 0.00172$).**

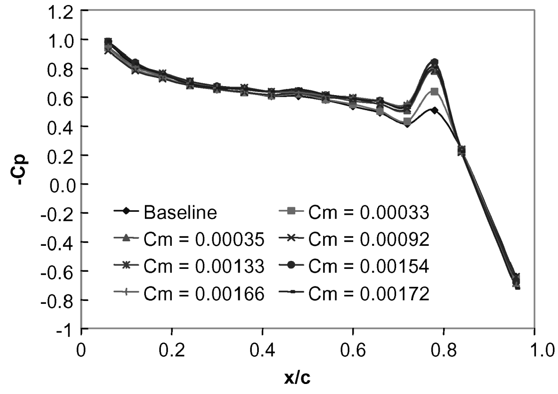

**Fig. 6 Pressure coefficient along the wing chord for varying suction rates at 4-deg angle of attack.**

and rolling moment increments due to actuation at each section are, respectively,

$$M_p = -F_l l_p \hat{\jmath} \tag{1a}$$

$$M_r = -F_l l_r \hat{\imath} \tag{1b}$$

A second coordinate system is chosen with its origin at the intersection of the center-of-pressure line and the vehicle plane of symmetry and its axis pointing outward coincident with the center-of-pressure line. Assuming that there are $N$ evenly spaced spanwise airfoil sections, the magnitude of the bias component of the net lift distribution is given by $a$, and the slope of the linearly varying component is given by $m$, we can now describe the lift forces generated by each spanwise airfoil segment. The distance of the center of pressure for the $i$th airfoil section from the inboard end of the controlled airfoil section, stated as the ratio to the overall length of the controlled airfoil section, is

$$x_i = (i-1)/(N-1) \tag{2}$$

The slope of the linearly varying component of the lift distribution is thus given by $m = (b - a)$, where $b$ is the magnitude of the distribution at the outboard end of the controlled portion of the airfoil.

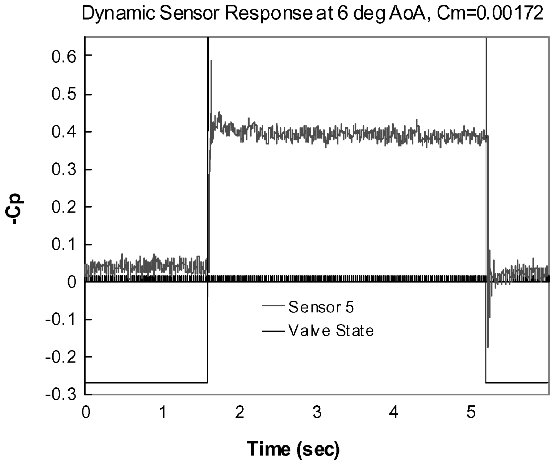

**Fig. 7 Time history for the pressure coefficient to stabilize after the actuator is turned on.**

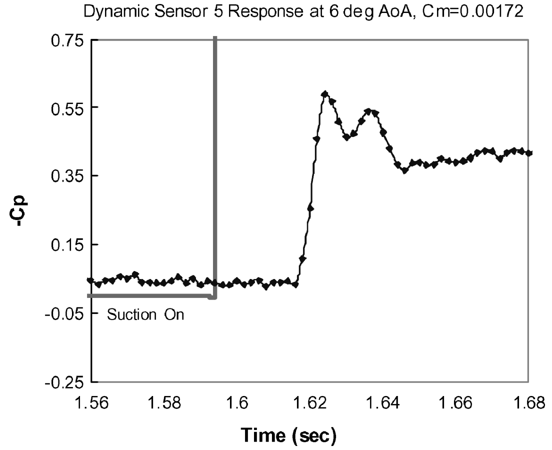

**Fig. 8 Time history for the pressure coefficient to stabilize after the actuator-on state.**

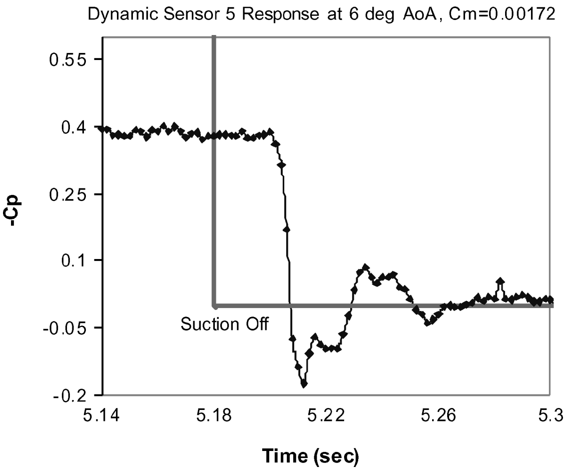

**Fig. 9 Time history for the pressure coefficient to stabilize after the actuator-off state.**

The magnitude of the lift force at the $i$th location is, therefore,

$$F_i = a + m x_i = a + [(i-1)/(N-1)](b-a) \tag{3}$$

The location of the center of pressure along the center-of-pressure line is given by

$$x_{\mathrm{cp}} = \frac{\sum_{i=1}^{N} F_i x_i}{\sum_{i=1}^{N} F_i} \tag{4}$$

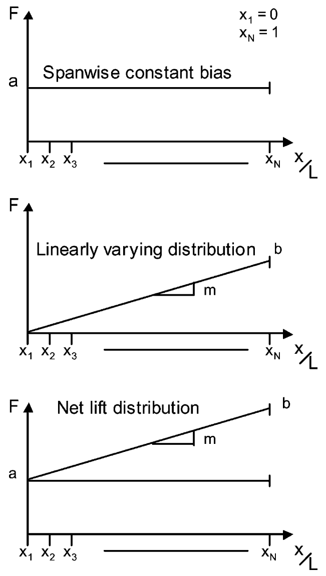

**Fig. 10 Shape functions: spanwise constant bias and linearly varying distribution.**

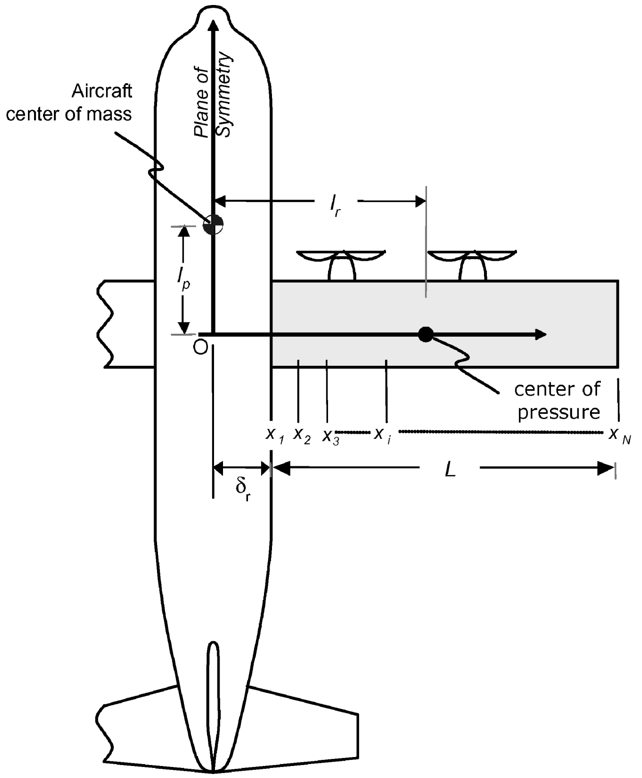

**Fig. 11 Vehicle schematic for GCS design.**

Substituting Eqs. (2) and (3) into Eq. (4) yields

$$x_{\mathrm{cp}} = \frac{1}{N-1} \frac{a \sum_{j=0}^{N-1} j + [m/(n-1)] \sum_{j=0}^{N-1} j^2}{Na + [m/(N-1)] \sum_{j=0}^{N-1} j} \tag{5}$$

and the net lift force is

$$F_l = \sum_{i=1}^{N} F_i = Na + \frac{m}{N-1} \sum_{j=0}^{N-1} j \tag{6}$$

Note that the net lift that can be produced is limited by the command authority of the flow-control devices.

Simple algebraic manipulation reveals that

$$\sum_{j=0}^{N-1} j = \sum_{j=1}^{N-1} j = \frac{N(N-1)}{2} \tag{7}$$

$$\sum_{j=0}^{N-1} j^2 = \sum_{j=1}^{N-1} j^2 = \frac{N(N-1)(2N-1)}{6} \tag{8}$$

Substituting Eqs. (7) and (8) into Eqs. (5) and (6) produces

$$F_l = \left(a + \frac{m}{2}\right)N, \qquad x_{\mathrm{cp}} = \frac{1}{(N-1)}\frac{(3a+2m)N-(3a+m)}{6a+3m} \tag{9}$$

or, in terms of $a$ and $b$,

$$F_l = \frac{(a+b)}{2}N \tag{10a}$$

$$x_{\mathrm{cp}} = \frac{1}{3(N-1)}\frac{(a+2b)N-(2a+b)}{a+b}$$

$$\Longrightarrow x_{\mathrm{cp}} = \frac{2}{3} + \frac{b-aN}{3(N-1)(a+b)} \tag{10b}$$

Recalling that the overall length of the airfoil's control section is $L$, the location of the center of pressure is given by

$$L_r = \delta_r + Lx_{\mathrm{cp}} \tag{11}$$

where $\delta_r$ is the distance between the aircraft's place of symmetry and the inboard end of the controller airfoil section. The pitch and roll moments about the vehicle center of mass are then given by

$$M_p = l_p N[(a+b)/2]$$

$$M_r = N(\delta_r + 2L/3)[(a+b)/2] + [N/(N-1)][(b-Na)L/6] \tag{12}$$

Noting that $L$ and $\delta_r$ are geometric constants and $N$ is a specified parameter, the following constants are defined:

$$C_1 = Nl_p/2, \qquad C_2 = N\delta_r/2 + N(N-2)L/6(N-1)$$

$$C_3 = N\delta_r/2 + N(2N-1)L/6(N-1), \qquad C_4 = N^2 L l_p\big/12 \tag{13}$$

Using these constants, the relationship between the lift magnitudes at the inboard and outboard ends of the control section, $a$ and $b$, respectively, and the rolling and pitching moments is given by the following linear mapping:

$$\begin{Bmatrix} M_p \\ M_r \end{Bmatrix} = \begin{bmatrix} C_1 & C_1 \\ C_2 & C_3 \end{bmatrix} \begin{Bmatrix} a \\ b \end{Bmatrix} \tag{14}$$

Applying Cramer's rule produces the inverse relationship

$$\begin{Bmatrix} a \\ b \end{Bmatrix} = \frac{1}{C_4} \begin{bmatrix} C_3 & -C_1 \\ C_2 & C_1 \end{bmatrix} \begin{Bmatrix} M_p \\ M_r \end{Bmatrix} \tag{15}$$

which can be used to determine the lift force distribution necessary to produce the desired moments. The current implementation uses this inverse relationship to compute a feedforward control input. A feedback loop can then be added to drive the moment error to zero. It must also be noted that the choice of shape functions used here reflect the linearity of the airfoil model and that other functions can be easily implemented. By combining multiple shape functions with a penalty function constraint, more than two shape functions can be made available to the GCS. In the absence of such a penalty function, the GCS is limited to at most two shape functions, and hence, the range of moments that can be generated by the controller are partially determined by the shape functions themselves. That is to say, the choice of any two shape functions for use in the GCS places constraints on the performance envelope in addition to those placed by the actuators themselves. This limitation can be ameliorated by the design of an optimal controller that admits more than two shape functions.

## V. Intelligent Control Modules

Using the shape functions, the GCS specifies a lift to be generated by each of the individual local airfoil sections. The ICMs then track the desired lift force trajectories for the individual airfoil sections. Figures 7–9 show the step response of the open-loop system at one of the sensor locations (sensor 5). Initial examination of the step responses at other sensor locations indicates that the dynamics remains constant over the surface of the airfoil and only the steady-state gain varies. Because the lift is computed by integrating $C_p$ over the airfoil surface, the net lift produced by an airfoil section may then be assumed to possess the same dynamics shown in Figs. 7–9, though the magnitudes of their respective lift contributions may vary. An input–output mapping between the suction coefficient, $C_m$, and the net lift generated by the airfoil section can be constructed by computing the steady-state gain via integration of steady-state gains of $C_p$ around the airfoil surface.

### A. Control Law Design

The open-loop system dynamics is modeled as a second-order linear system with an integer delay. The open-loop transfer function for a second-order linear system is

$$G(s) = K\big/\left(s^2\big/\omega_n^2 + 2\xi s/\omega_n + 1\right) \tag{16}$$

where $K$ is the steady-state gain and $\omega_n$ and $\xi$ are the natural frequency and damping ratio of the system, respectively. All of these parameters are obtained from the experimental open-loop step responses such as the one shown in Fig. 7.

Using adaptive control techniques has the benefit of imbuing the controller with the ability to adapt to changing system dynamics. In the present case, the system dynamics is also a function of the angle of attack and freestream velocity. The adaption mechanism allows the controller to effectively regulate the flow-control device throughout its performance envelope without a deterioration of performance. To this end, an STR is examined. Digital control techniques were chosen for the ease they provide for modeling delays and to avoid the difficulties inherent in force feedback systems, namely a lack of derivative information. In addition, a digital implementation provides a model form that can be easily used to design an adaptive controller. A zero-order hold model was used to produce a discrete transfer function of the continuous time model,

$$G(z) = \frac{z-1}{z} Z\left\{\frac{G(s)}{s}\right\}$$

$$= \frac{K(Az+B)}{z^2 - 2e^{-\xi\omega_n T}\left(\cos\omega_n\sqrt{1-\xi^2}\right)z + e^{-2\xi\omega_n T}} \tag{17}$$

where $T$ is the sampling period and

$$A = 1 - e^{-\xi\omega_n T}\cos\omega_n\sqrt{1-\xi^2} - \frac{\xi}{\sqrt{1-\xi^2}}e^{-\xi\omega_n T}\sin\omega_n\sqrt{1-\xi^2}$$

$$B = e^{-2\xi\omega_n T} + \frac{\xi}{\sqrt{1-\xi^2}}e^{-\xi\omega_n T}\sin\omega_n\sqrt{1-\xi^2}$$

$$- e^{-\xi\omega_n T}\cos\omega_n\sqrt{1-\xi^2}$$

Applying a $p$-step delay to the system produces

$$G(z) = \frac{K(Az+B)}{z^p\left(z^2 - 2e^{-\xi\omega_n T}\left(\cos\omega_n\sqrt{1-\xi^2}\right)z + e^{-2\xi\omega_n T}\right)} \tag{18}$$

Figure 12 shows the open-loop step response of this model, and Fig. 13 depicts a detail from the open-loop step response showing the delay in the model. The parameters used in the model are obtained from the step-response data shown in Figs. 7–9. The open-loop gain is normalized by the steady-state lift increment produced by a unit suction input. As noted previously, the lift produced over different wing sections may vary in magnitude though the essential dynamics remain the same. The normalize response provides a useful construct for automating the ICM control law design process for the different airfoil sections. The delay in the model is significantly

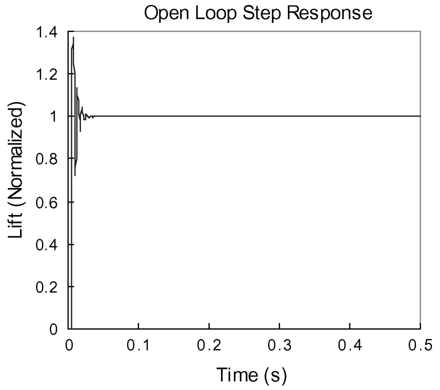

**Fig. 12 Open-loop step response of the model.**

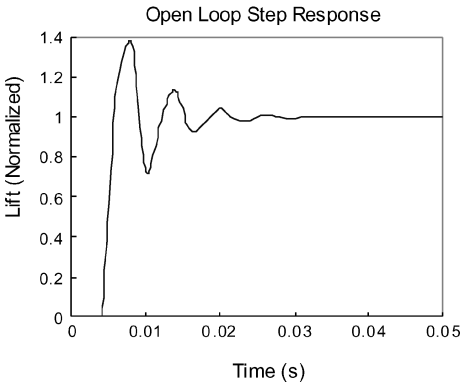

**Fig. 13 Open-loop step response showing the delay in the model.**

smaller than the delay seen in the original system. It is believed that the delay in the original system is primarily an artifact of the length of the tubing used to supply the suction in the experiment and would be significantly shorter in an actual implementation. For this reason, a shorter delay ($\tau_d = 0.004$ s vs $\tau_d = 0.02$ s) that is scaled linearly to reflect the shorter tubing that would be used in application is used in the model. Because a linear model is being used to represent the system behavior, the presence of a larger delay can be accommodated very simply via this design methodology, though the closed loop system response will reflect the larger delay.

This model is then restated in terms of the shift operator, $q$, to yield

$$G(q) = \frac{B(q)}{A(q)} = \frac{b_1 q + b_0}{q^{p+2} + a_{p+1}q^{p+1} + a_p q^p} \tag{19}$$

where the coefficients of $q$ are identical to the coefficients of $z$. This model, form is known as an ARMA model, where the polynomial $A(q)$ contains autoregressive (AR) information and the polynomial $B(q)$ contains moving average (MA) information. Note also that the model formulation given by Eq. (19) is valid for any $p$-step delay.

One method of designing STRs is to specify desired closed-loop dynamics, referred to as the model dynamics,

$$G_m(q) = B_m(q)/A_m(q) \tag{20}$$

and the pole placement algorithm can be used to design a feedback regulator of the form

$$R(q)u(t) = T(q)u_c(t) + S(q)y(t) \tag{21}$$

With this controller, the closed-loop system can be represented as

$$y(t) = [BT/(AR + BS)]u_c(t) + [BR/(AR + BS)]v(t)$$
$$u(t) = [AT/(AR + BS)]u_c(t) - [BS/(AR + BS)]v(t)$$

and the closed-loop characteristic polynomial is, therefore,

$$AR + BS = A_0 A_m B^+ \tag{22}$$

where $A_0$ is the observer and $B^+$ is the polynomial containing the stable zeros of the open-loop system. This is a Diophantine equation (Bezout identity) and can be easily solved in real time.

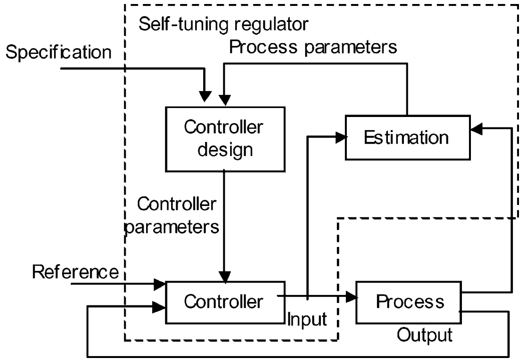

**Fig. 14 STR block diagram.**

### B. System Identification

An STR can be separated into two loops: the inner (plant feedback controller) loop and the outer (parameter estimator/design) loop, as shown in Fig. 14. The outer loop is dependent on a least-squares estimate that is used to provide system parameters for updating the regulator parameters. The controller design block accepts the input from the estimator as well as a specification of the desired system dynamics. The results given by the process estimation block are assumed to be perfect estimates in accordance with the certainty equivalence principle and are used to calculate a solution to the underlying design problem. This solution is then use to update the controller parameters for the inner loop.

In the implementation examined here, the controller updates parameters at every sampling period and hence the estimation block in Fig. 14 identifies the coefficients of the transfer function model given by Eq. (19) in real time via recursive least-squares (RLS) estimation. Because the model parameters are expected to change with the flow conditions over the airfoil and, therefore, with time, exponential forgetting is incorporated into the RLS estimator to discount older data. In an RLS estimator with exponential forgetting, model parameters are based on the average behavior of the plant dynamics, using the least-squares criterion:

$$V(\boldsymbol{\theta}, t) = \frac{1}{2}\sum_{i=1}^{t} \lambda^{t-i}[y(i) - \boldsymbol{\varphi}^T(i)\boldsymbol{\theta}]^2 \tag{23}$$

where $y$ is the observed variable, $\boldsymbol{\theta}$ represents the vector of parameters to be determined, and $\boldsymbol{\varphi}$ is the vector of regressors being used, and $\lambda$ is the forgetting factor. The parameter vector $\boldsymbol{\theta}$ is determined to minimize the least-squares criterion, Eq. (23).

If a process is given as

$$y(i) = \boldsymbol{\varphi}^T(i)\boldsymbol{\theta}^0 + e(i) \tag{24}$$

where is the vector of certain parameters and $\{e(i), i = 1, 2, \ldots\}$ is a sequence of independent, equally distributed random variables with zero mean, then an RLS estimation can be formulated as follows.

If the matrix

$$\Phi(t) = \begin{bmatrix} \varphi^T(1) \\ \vdots \\ \varphi^T(t) \end{bmatrix} \tag{25}$$

has full rank for all $t \geq t_0$ then, given $\hat{\theta}(t_0)$ and $\hat{\theta}(t_0)P(t_0) = [(\Phi^T(t_0)\Phi(t_0)]^{-1}$, the least-squares estimate $\hat{\theta}(t)$ satisfies the recursive equations

$$\hat{\theta}(t) = \hat{\theta}(t-1) + K(t)[y(t) - \varphi^T(t)\hat{\theta}(t-1)]$$
$$K(t) = P(t)\varphi(t) = P(t-1)\varphi(t)[\lambda I + \varphi^T(t)P(t-1)\varphi(t)]^{-1}$$
$$P(t) = [I - K(t)\varphi^T(t)]P(t-1)/\lambda \tag{26}$$

which can be interpreted as a Kalman filter for the process

$$\theta(t+1) = \theta(t), \qquad y(t) = \varphi^T(t)\theta(t) + e(t)$$

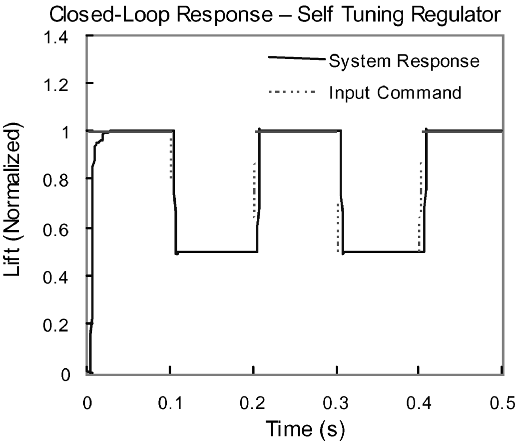

**Fig. 15 Closed-loop response of the model.**

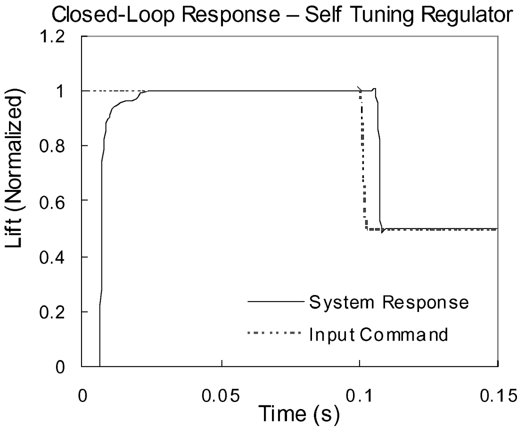

**Fig. 16 Closed-loop response showing delay in the model.**

### C. Controller Tuning

Once RLS estimation is completed, model-based tuning proceeds with controller design using the identified model. The pole placement design algorithm given by Eq. (22) is used to obtain the parameters for the regulator described by Eq. (21). In the implementation discussed here, the desired dynamics has been chosen to possess the same structure as that of the system model given by Eq. (16) but with $\omega = \sqrt{2}\omega_n$, $\xi = 0.6$, and $K = 1$ and a second-order observer $A_0 = (q^{-1} - 0.5)^2$ is used to complete the controller specification. A unit steady-state gain, $K$, is used so that a generic structure can be developed for the ICMs.

The STR design also assumes a unity steady-state gain for the system model representing the mapping between the applied suction and the lift produced over a wing section. The actual gain will vary from airfoil section to airfoil section but the generic system described earlier can be easily customized for each section by scaling it with the appropriate gain. An exponential forgetting factor of $\lambda = 0.18$ has been chosen experimentally for the RLS parameter estimation.

The closed-loop step response of the model is depicted in Figs. 15 and 16. Figure 17 shows the control input to the system. The control input shows a significant amount of ringing. This ringing is the result of the system delay and the elimination of a stable but lightly damped zero (hence the implicit cancelation of a lightly damped pole). A redesign of the structure of the desired closed-loop dynamics such that the zero is not canceled should mitigate this problem. Finally, Fig. 18 shows the parameter adaption. The initial model parameters are specified to be 25% higher than the actual model parameters. As can be seen, the regulator quickly converges to the true values.

**Table 1 Simulation parameters (Tu-144 aircraft)**

| Parameter | Value |
|---|---|
| Length | 60.0 m |
| Span | 27.0 m |
| Nose tip to leading edge of MAC | 30.1 m |
| Length of MAC | 23.3 m |
| Wing area | 438 $\mathrm{m}^2$ |
| Wing aspect ratio | 1.66 |
| Wing sweep, inboard portions | 76 deg |
| Wing sweep, main panels | 57 deg |
| Weight | 138,000 kg |
| Roll axis moment of inertia, $I_{xx}$ | 1,635,000 kg · $\mathrm{m}^2$ |
| Pitch axis moment of inertia, $I_{yy}$ | 17,606,000 kg · $\mathrm{m}^2$ |
| Yaw axis moment of inertia, $I_{zz}$ | 18,973,000 kg · $\mathrm{m}^2$ |
| Roll-Yaw product of inertia, $I_{xz}$ | −273,000 kg · $\mathrm{m}^2$ |

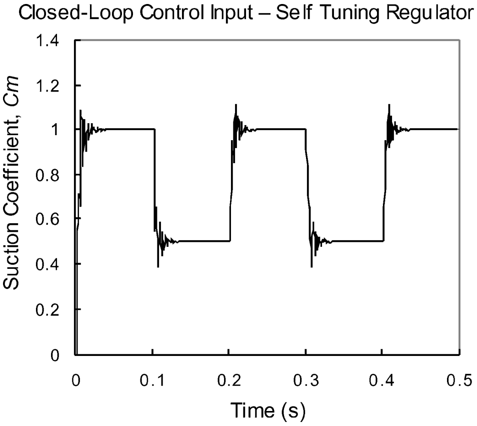

**Fig. 17 Closed-loop control input to the system.**

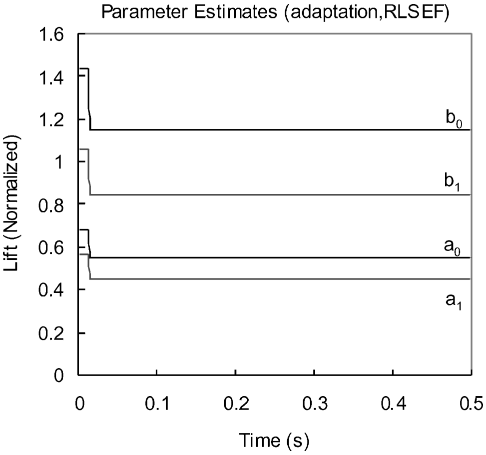

**Fig. 18 STR parameter adaption.**

## VI. Simulation of the Global Control System

The prequel details the development of an STR for the ICMs as well as the preliminary development of a GCS to coordinate the ICMs. In this section, simulation results that validate the feasibility of the overall control architecture are presented.

The simulation uses a full, six-degree-of-freedom (DOF) rigid-body model of an aircraft whose right wing is populated with ICMs and a desired moment trajectory is specified for both the rolling and pitching moments in the simulations. The Tu-144 model is used for this simulation because its aerodynamic data are readily available in the open literature. The geometric and inertial properties used are given in Table 1. It should be noted that the lift characteristics of the wings used in the simulation are based on the lift characteristics of the two-dimensional airfoil used in our experimentation and are scaled to match the reference area of the Tu-144 aircraft flying at Mach 0.35.

The lift characteristics of the wing used in our experiments were clearly different from those of the Tu-144 because it produces less lift. The moments produced by the modulation of the lift distribution are therefore underpredicted. The right wing is divided into 10 sections, each of which can modulate the lift produced. A continuous-time model of the ICM is incorporated at each of the wing sections and is used to determine the actual lift produced by each wing section.

Data taken for the experimental wing are used to determine the baseline (no suction applied) and maximum lift that the wing sections are capable of producing over a range of angles of attack from 4 to 6 deg. Interpolation using cubic Hermite interpolants was used to determine the model parameters for the ICMs as the aircraft's orientation changes in response to the applied forces and moments. In addition, the effects of actuator saturation are incorporated into the models of the ICMs. The ICMs cannot decrease the lift below the baseline lift nor can they produce more than the maximum experimentally measured lifts. The actual forces produced by each wing section are applied independently to the rigid-body model of the aircraft.

Figure 19 shows the trajectory tracking response of the GCS. In this case, both pitching and rolling moments begin by tracking the maximum proportional trajectories possible; that is, the specified lift distribution consists solely of a constant bias whose magnitude is equal to the maximum lift that can be specified. At time $t = 0.2$, the desired rolling moment is changed while the pitching moment is held constant; then at time $t = 0.3$, the desired pitching moment is varied while the rolling moment is held constant. As can be seen, when the desired trajectories are proportional, the GCS performs well. However, when the moments are varied independently, the performance degrades. This is a consequence of actuator saturation and the shape functions used to construct the lift distribution. To exactly track the desired trajectories, the current shape functions require that the ICMs be capable of decreasing the lift of a section. It is believed that a better selection of shape functions can ameliorate this limitation.

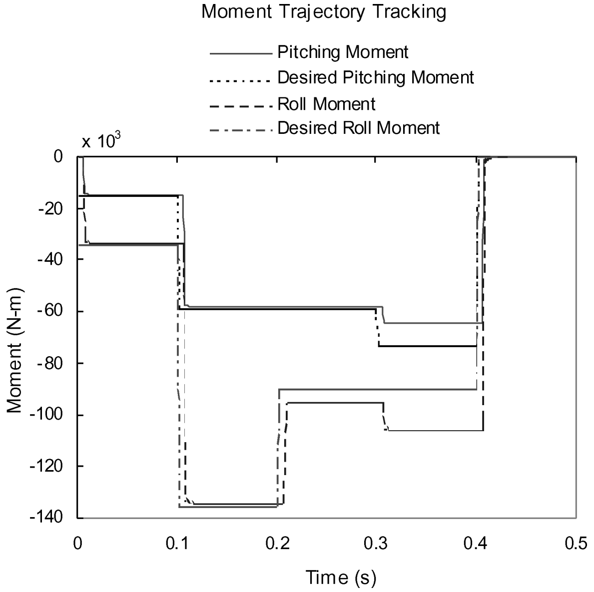

**Fig. 19 Moment trajectory tracking.**

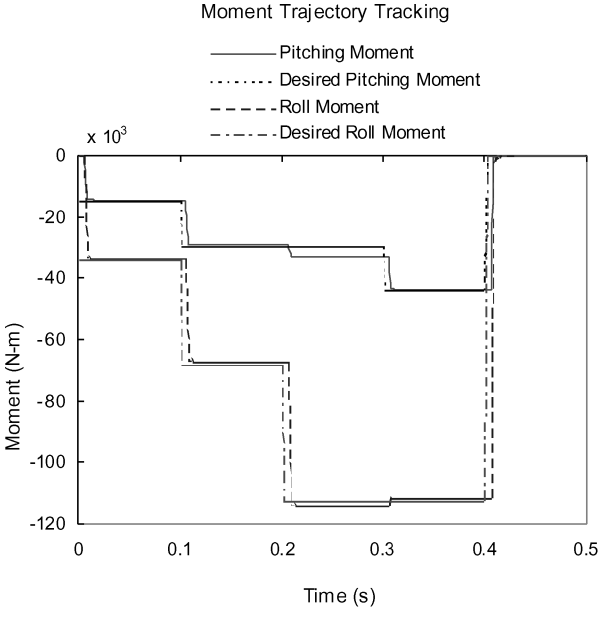

**Fig. 20 Moment tracking, small moments.**

Figure 20 shows the same trajectory information for smaller desired moments. As can be seen, the performance is much better because the effects of actuator saturation are mostly avoided. The simulation results demonstrate the feasibility of independently modulating the pitch and rolling moments within some performance envelope and suggest that the increase in actuator capability (i.e., the ability to produce more suction or to produce both blowing and suction) will greatly increase the size of the performance envelope. In addition, a more careful selection of shape functions and the addition of additional shape functions with a penalty constraint will allow a much larger range of moments to be modulated.

## VII. Conclusions

The feasibility of a modular closed-loop flow-control approach for aerodynamic shaping of air vehicles using ICMs coupled with a GCS has been shown. Specifically, the effectiveness of ICMs for the control of local flow phenomena has been demonstrated via wind-tunnel experiments and coordination of the ICMs by a GCS has been numerically simulated using a six-DOF aircraft model. The presented simulation results illustrate the capability of the hierarchical control system to track desired moment trajectories about the aircraft's center of mass using active flow-control devices.

## Acknowledgments

The authors acknowledge the support of the U.S. Air Force Research Laboratory (AFRL), Wright–Patterson Air Force Base (WPAFB), under contract grant F33615-02-M-3227. Special thanks go to Chris Camphouse and Carl Tilmann of AFRL, WPAFB, for their continued support and encouragement of this work.

## References

[1] Smith, B. L., and Glezer, A., "The Formation and Evolution of Synthetic Jets," *Physics of Fluids*, Vol. 10, No. 9, 1998, pp. 2281–2297.

[2] Wygnanski, I., "Boundary Layer and Flow Control by Periodic Addition of Momentum," AIAA Paper 1997-2117, June–July 1997.

[3] Patel, M. P., Tilmann, C. P., and Ng, T. T., "Active Transparent Stall Control System for Air Vehicles," *Journal of Aircraft*, Vol. 40, No. 5, 2003, pp. 993–997.

[4] Magill, J. C., and McManus, K. R., "Control of Dynamic Stall Using Pulsed Vortex Generator Jets," AIAA Paper 1998-0675, Jan. 1998.

[5] Ng, T. T., and Lang, Y., "Shear Layer Instability Induced Separation Control," *AIAA Journal*, Vol. 37, No. 3, 1999, pp. 386–388.

[6] Högberg, M., Bewley, T. R., and Henningson, D. S., "Linear Feedback Control and Estimation of Transition in Plane Channel Flow," *Journal of Fluid Mechanics*, Vol. 481, 2003, pp. 149–175.

[7] Gunzburger, M. D., and Manservisi, S., "Analysis and Approximation of the Velocity Tracking Problem for Navier–Stokes Flows with Distributed Control," *SIAM Journal on Numerical Analysis*, Vol. 37, No. 5, 2000, pp. 1481–1512.

[8] Lee, C., Kim, J., Babcock, D., and Goodman, R., "Application of Neural Network to Turbulence Control for Drag Reduction," *Physics of Fluids*, Vol. 9, No. 6, 1997, pp. 1740–1747.

[9] Patel, M. P., Lisy, F. J., Prince, T. S., Ng, T. T., DiCocco, J. M., and Carver, R., "Active Flow Control for Aerodynamic Enhancement," Air Force Research Laboratory, AFRL-VA-WP-TR-2001-3061, Wright–Patterson AFB, OH, Nov. 2001.

[10] Åström, K. J., and Wittenmark, B., *Adaptive Control*, Addison Wesley, Reading, MA, 1989.

[11] Ng, T. T., and Osborn, R., "Active Control of Leading Edge Separation," American Society of Mechanical Engineers, Paper FEDSM99-6918, July 1999.

[12] Ng, T. T., and Osborn, R., "Control of Leading Edge Separation Using Discrete Suction," AIAA Paper 2000-0651, Jan. 2000.

[13] Patel, M. P., Skebe, G., Ng, T. T., and Lisy, F. J., "Development of a MEMS Based Microvalve for Flow Control Using Active Dimples," AIAA Paper 2002-0270, Jan. 2002.